Volume 11
Number 5
7 February 2023
Pages 2057–2484

Journal of Materials Chemistry A

Materials for energy and sustainability

rsc.li/materials-a

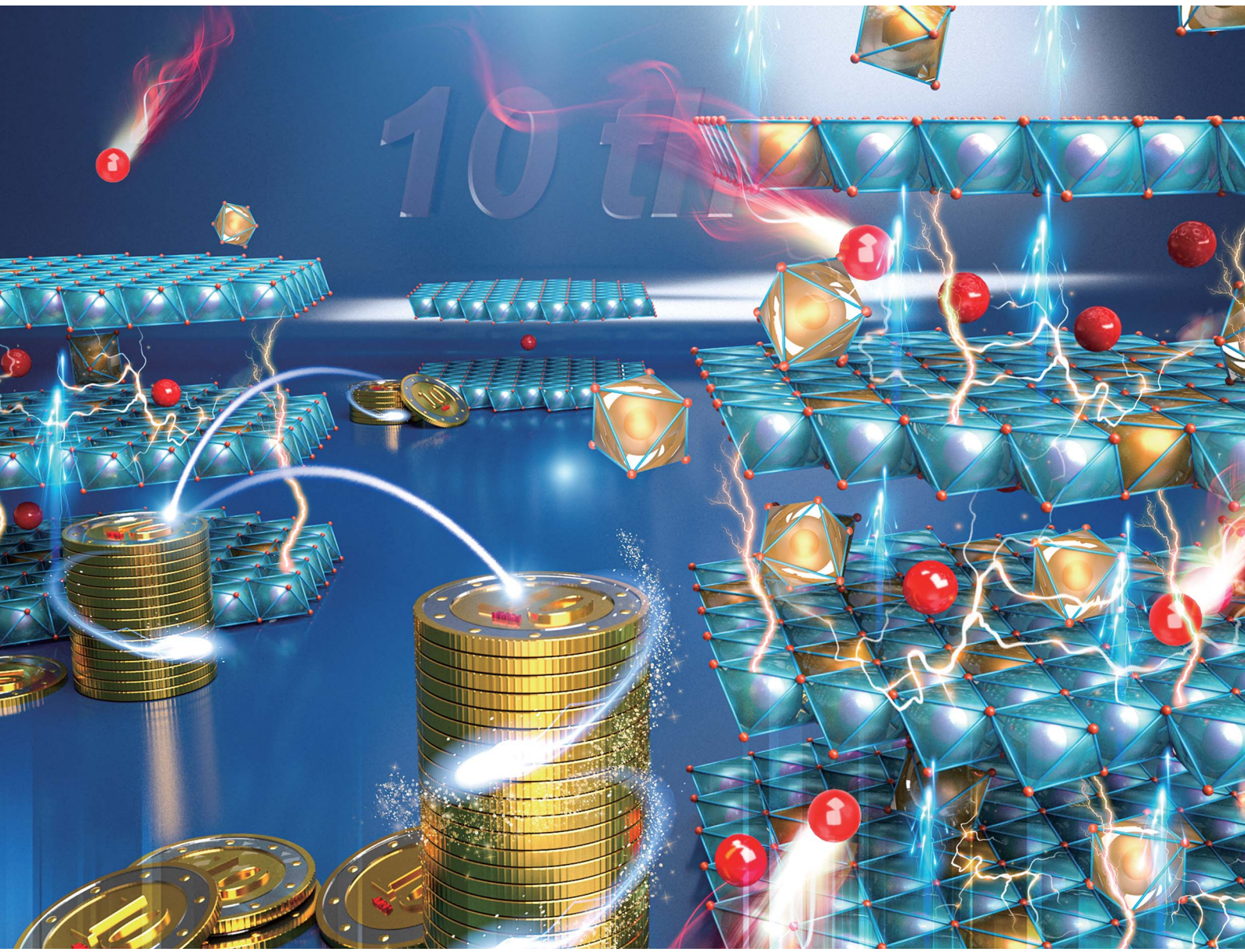

ISSN 2050-7488

ROYAL SOCIETY OF CHEMISTRY

PAPER

Lei Zhao, Junjie He *et al.*

Improving the intrinsic conductivity of δ-MnO_2 by indium doping for high-performance neutral aqueous sodium-ion supercapacitors with commercial-level mass-loading

10 YEARS ANNIVERSARY

Journal of Materials Chemistry A

ROYAL SOCIETY OF CHEMISTRY

PAPER

View Article Online
View Journal | View Issue

Check for updates

Cite this: J. Mater. Chem. A, 2023, 11, 2133

Improving the intrinsic conductivity of δ-MnO_2 by indium doping for high-performance neutral aqueous sodium-ion supercapacitors with commercial-level mass-loading†

Borui Li,‡[ab] Yanfang Chu,‡[a] Bin Xie,[a] Yuchen Sun,[a] Lin Zhang,[a] Hongmei Zhao,[c] Lei Zhao,*[c] Peng-Fei Liu[d] and Junjie He*[ac]

Received 4th November 2022
Accepted 23rd December 2022

DOI: 10.1039/d2ta08638g

rsc.li/materials-a

Published on 24 Aralk 2022. Downloaded on 9.07.2024 15:25:36.

Due to their potential use in energy storage and next-generation water purification devices, neutral aqueous supercapacitors (NASCs) have attracted significant attention from researchers. δ-MnO_2 is a well-known cathode material for supercapacitors due to its 2D structure and high capacitance. However, its poor conductivity limits the mass loading on the electrode. Moreover, the dissolution of δ-MnO_2 hampers its cycling stability and applicability in water purification. Here, indium is introduced to δ-MnO_2 with the aid of iron. The crystal water and conductivity of the δ-MnO_2 are significantly influenced by indium. After optimization of the concentration of indium in δ-MnO_2, the gravimetric capacitance of δ-MnO_2 increases to 1302 F g^{-1} (95% of the theoretical limit). At a mass loading of 10.6 mg cm^{-2}, 180 F g^{-1}, 1.9 F cm^{-2} and 54 F cm^{-3} at 10 mA cm^{-2} can be obtained. A NASC (In doped δ-MnO_2//active carbon) exhibits a maximum areal energy density of 0.55 mW h cm^{-2} and a volumetric energy density of 18.7 mW h cm^{-3} at an areal power density of 1.0 mW cm^{-2}. 90% capacitance retention after 13 000 cycles arises from the prevention of Jahn–Teller distortion. First principles calculations and experimental results demonstrate that In doping is effective in enhancing the intrinsic properties of δ-MnO_2. These findings open up a new path towards high-performance supercapacitors.

1 Introduction

Neutral aqueous supercapacitors (NASCs) are a hot topic that has attracted widespread attention from scientists, not only because of their application as high-performance energy storage equipment for the environmentally-friendly collection of energy *via* geothermal, solar, and tidal methods, but also for their recent development as potential novel water-purification devices.[1–9] Supercapacitors have outstanding charging and discharging rates and excellent long-term cycling performance, which are superior to those of other energy storage components.[10,11] Usually, supercapacitors are composed of cathodes and anodes, which are made from suitable materials.[12,13] To date, despite the existence of traditional carbon materials based on electric double-layer capacitance,[14,15] many kinds of pseudocapacitive materials that function based on reduction–oxidation (redox) reactions have been developed.[16] These pseudocapacitive materials have much higher energy density than electric double-layer capacitors (EDLC). Conductive polymers and different transition metal oxides have been utilized as pseudocapacitive materials.[17,18]

Manganese dioxide is an attractive material for energy storage due to the low cost and high natural abundance of manganese.[19,20] Among the different forms of manganese dioxide, delta phase manganese dioxide (δ-MnO_2) has been extensively studied over the past few decades because of its two-dimensional (2D) layered structure benefiting ion diffusion.[21–24] Two main issues limit the practical application of δ-MnO_2 based aqueous supercapacitors, including inferior structural stability and the drastic fading of gravimetric capacitance when the mass loading is higher than 0.5 mg cm^{-2}. Making up for these shortcomings is even more critical for its application in water purification. It is believed that Jahn–Teller distortion of Mn^{3+} is the main reason for the instability. The poor electronic conductivity (10^{-5}–10^{-6} S cm^{-1}) of δ-MnO_2 leads to limitations in mass loading, although its high gravimetric capacitance

[a]Biomass New Materials Research Center, College of Architectural Engineering, Yunnan Agricultural University, Kunming 650201, China. E-mail: junjiehe@ynau.edu.cn

[b]Department of Chemical and Environmental Engineering, University of Nottingham Ningbo China, Ningbo 315100, China

[c]Yunnan International Joint Research and Development Centre for Smart Agriculture and Water Security, Yunnan Agricultural University, Kunming 650201, China. E-mail: zhaolei928@ynau.edu.cn

[d]Spallation Neutron Source Science Center, Institute of High Energy Physics, Chinese Academy of Sciences, Dongguan 523803, China

† Electronic supplementary information (ESI) available. See DOI: https://doi.org/10.1039/d2ta08638g

‡ These authors contribute equally to this work.

Published on 24 Aralk 2022. Downloaded on 9.07.2024 15:25:36.

approaches the theoretical limit (TL, 1370 F g^{-1}).[25] Utilization of a nanoporous gold electrode, 1145 F g^{-1} (84% of TL), was reported in 2011.[26] Carbon nanotube sponge hybrid electrodes show a gravimetric capacitance of up to 1230 F g^{-1} (90% of TL). Unfortunately, this high gravimetric capacitance can only be obtained while the mass loading is lower than 0.2 mg cm^{-2}, which is far from the requirements of commercialization (>5 mg cm^{-2}).[27,28] So far, to boost the performance of δ-MnO_2 electrodes with high mass loading, many novel nano technologies have been developed to provide porous electrodes to allow an ultrathin δ-MnO_2 layer to facilitate electron and ion transport.[25,29–33] Recently, Choi *et al.* developed a δ-MnO_2 and nitrogen-doped carbon composite, of which high gravimetric and areal capacitances of 480.3 F g^{-1} and 9.4 F cm^{-2} at 0.5 mA cm^{-2} were achieved, respectively, when an ultrahigh mass loading of 19.7 mg cm^{-2} was applied.[34] Similarly, the grafting of δ-MnO_2 on carbon nanotubes, graphene and conductive nanoneedle arrays, *etc.*, are also beneficial for the high mass loading of NASCs.[35–37]

However, improving the intrinsic performance of δ-MnO_2 is still attractive due to the fundamental role of δ-MnO_2 in related NASCs.[38] Besides this, the Jahn–Teller distortion of Mn^{3+} needs to be prevented by optimizing the electronic structure of δ-MnO_2. Doping has proved to be a very effective way to enhance the electron and ion conductivity of δ-MnO_2. Fe, Ag, Au, Ce, Bi, Al, Mg, and Zn[39–46] have been introduced into δ-MnO_2 with different crystal structures. In 2020, Xia's group reported that 2 mol% Cr-doped δ-MnO_2 exhibited a high capacitance of 250 F g^{-1} at 0.2 A g^{-1} and 150 F g^{-1} at 10 A g^{-1} (5 mg cm^{-2} mass loading).[47] Moreover, the introduction of Cr prevented the dissolution of δ-MnO_2 to result in outstanding long term cycling stability. To date, we have had to face the fact that the poor conductivity of δ-MnO_2 still hinders the specific capacitance of δ-MnO_2 at high mass loading, but fewer and fewer elements are left for doping. Some elements cannot be introduced into δ-MnO_2 due to structural limitations or defect toleration of δ-MnO_2 crystals. Thus, how to enhance the intrinsic performance of δ-MnO_2 is still a challenge.

Herein, we report an indium (In) doping method to improve the electron and ion conductivity of δ-MnO_2. We found that In could not be doped directly into δ-MnO_2. The introduction of In (0.7 mol%) with 5 mol% Fe dopant increased the electron conductivity of δ-MnO_2 from $\sim 10^{-6}$ to 10^{-5} S cm^{-1}. On carbon cloth (CC), the mesoporous flower-like structure and weakened binding energy facilitate the ion diffusion in Fe–In doped δ-MnO_2. These advantages push the record of gravimetric capacitance of δ-MnO_2 to 1302 F g^{-1} (95% of TL) in neutral Na_2SO_4 aqueous solution. When the mass loading increased to 10.6 mg cm^{-2}, 180 F g^{-1}, 1.9 F cm^{-2} and 54 F cm^{-3} at 1.0 A g^{-1} (10 mA cm^{-2}) were obtained by using commercial carbon cloth without any ancillary nanotechnologies. The introduction of Fe–In simultaneously enhanced the structural stability of δ-MnO_2. No capacitance degradation of Fe–In doped δ-MnO_2 was observed after 12k cycles in 1 M Na_2SO_4 aqueous solution. An aqueous asymmetric supercapacitor (ASC) was fabricated by incorporating the Fe–In doped δ-MnO_2 with optimized composition in commercially available active carbon (AC), the resulting product of which exhibits a maximum areal energy density of 0.55 mW h cm^{-2} and a volumetric energy density of 18.7 mW h cm^{-3} at an areal power density of 1.0 mW cm^{-2}. A volumetric energy density of 13.0 mW h cm^{-3} was obtained at an areal power density of ∼30 mW cm^{-3}. This high mass loading device showed 90% capacitance retention after 13 000 cycles. Theoretical calculation and experimental results demonstrated that the novel Fe–In doping method is an effective way to enhance the intrinsic properties of δ-MnO_2 materials.

2 Results and discussion

The overall content of the work, involving the enhancement of the conductivity and diffusion of sodium ions of δ-MnO_2, and the nanoflower structure induced by indium doping, is depicted in Fig. 1. It has been widely accepted that the low experimental capacitance of δ-MnO_2 arises from its poor conductivity and ion diffusion in materials.[48,49] The present work improves the intrinsic conductivity of δ-MnO_2 *via* the introduction of Fe and In as dopants. A δ-MnO_2 nanoflower structure is observed (Fig. 1(c)) and has a loose texture that facilitates ion diffusion when the In content is optimal. To carefully estimate the influences of dopants on the capacitance of δ-MnO_2, samples were prepared from the related solutions with different reactants, including no dopant (PMO), 5 mol% Fe doping (FeMO), and x mol% In plus 5 mol% Fe doping (x% InFeMO).

After deposition, the carbon fibers (CF) of CC are covered with a layer of δ-MnO_2, of which the morphology varies according to the different dopant composition. PMO and FeMO densely cover the CF, while the nanoflower morphology becomes clearer upon increasing the In concentration (Fig. 2(a–e) and S1†). High-resolution transmission electron microscopy (HRTEM images, Fig. 2(f–j)) were also obtained. Well-resolved lattice fringes with an interspacing of ∼0.26 nm and ∼0.34 nm corresponding to (101) and (110) facets of birnessite ($Na_xMnO_2 \cdot yH_2O$) were observed, respectively.[50] From the electron diffraction patterns of the dim fringe spacing in the corresponding selected area, PMO shows the poorest crystallinity. The addition of Fe and In improves the crystallinity of δ-MnO_2 to present sharp diffraction spots (insets in Fig. 2(f–j)). Meanwhile, a lot of diffraction spots are observed in Fig. 2(j) due to the formation of impure phases, which is confirmed by the X-ray diffraction (XRD) data. Energy dispersive X-ray spectroscopy (EDS) elemental mapping images of Mn, Fe, In, and Na are shown at the bottom of Fig. 2 and S2.† The distribution of all elements are homogenous on the surface of CF, indicating that the elements are introduced into the structure of δ-MnO_2 crystal rather than forming impurities.

As shown in Fig. 3(a), the diffraction peaks can be well indexed to birnessite $Na_xMnO_2 \cdot yH_2O$ (PDF no. 43-1456) when 5 mol% of Fe and less than 0.7 mol% of In are doped into δ-MnO_2. The peak at 12° corresponds to the (001) facet. For all samples, this peak is broadened. The low crystallinity of all samples and the variable concentration of sodium ions between the facets led to the wide distribution of the distance between the (001) facets and the broad peaks. This can be interpreted as

 This journal is © The Royal Society of Chemistry 2023

Published on 24 Aralk 2022. Downloaded on 9.07.2024 15:25:36.

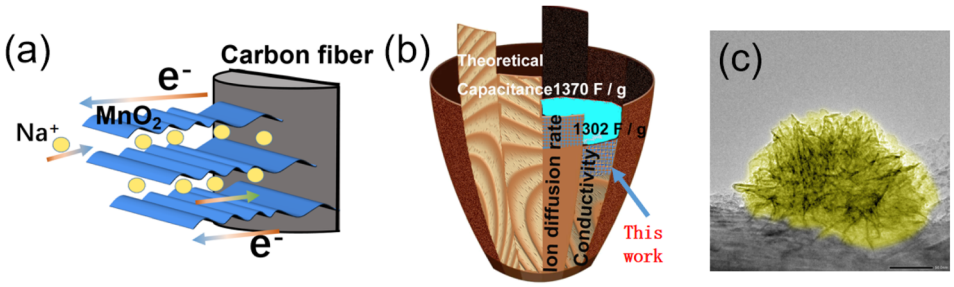

Fig. 1 (a) Schematic illustration of the flow of ions and electrons on a δ-MnO_2/CC electrode. (b) The poor conductivity as a short board of δ-MnO_2 for supercapacitors. (c) A SEM image of a δ-MnO_2 nanoflower on carbon fiber.

with the enhanced crystallinity of the samples, the diffraction intensity increases with the increasing In dopant concentration, which is consistent with the transmission electron microscopy (TEM) results. However, the higher doping concentration of In leads to the formation of indium oxide (PDF no. 06-0416), as indicated by the peak at 30.8°. Here, we believe it is necessary to report that In cannot be introduced into δ-MnO_2 without Fe. If 0.7 mol% of In is added to the solution in the absence of 5 mol% of Fe, a strong impurity phase peak indexed to $InMnO_3$ (PDF no. 50-0447) at 15.8° is observed in the top curve in Fig. 3(a). This means that In cannot substitute the Mn atoms in the birnessite crystal structure directly even at a very low concentration. To further investigate the influence of In doping on the crystal structure, the Raman spectra of PMO, FeMO, 0.35% InFeMO, 0.7% InFeMO and 1.4% InFeMO were recorded, with the results shown in Fig. 3(b). The broad peaks located at 600–645 cm^{-1} are characteristic peaks corresponding to the Mn–O bond symmetric stretching vibrations of MnO_6 octahedra.[51,52] According to Hooke's law, the blue shifting of the peaks of all In-doped samples can be attributed to an increase in the force constant.[52–55] This indicates that the introduction of In into birnessite is beneficial to reinforcing its structure. The trend in the Mn–O bond strength is consistent with the trend in the charge/discharge cycling stability of the corresponding electrodes. All of the In-doped samples exhibit higher intensity sharper characteristic peaks than those of the materials without In, which can be attributed to the reinforced structure and better crystallinity of the In-doped materials. The elemental composition of the materials was studied by inductively coupled plasma mass spectrometry (ICP-MS). In Fig. 3(c), the Fe concentration is 0.3% higher than the Fe added into the reactants, which can be attributed to the raw material manganese acetate as a small amount of Fe can be introduced into the raw materials easily during the production process of manganese

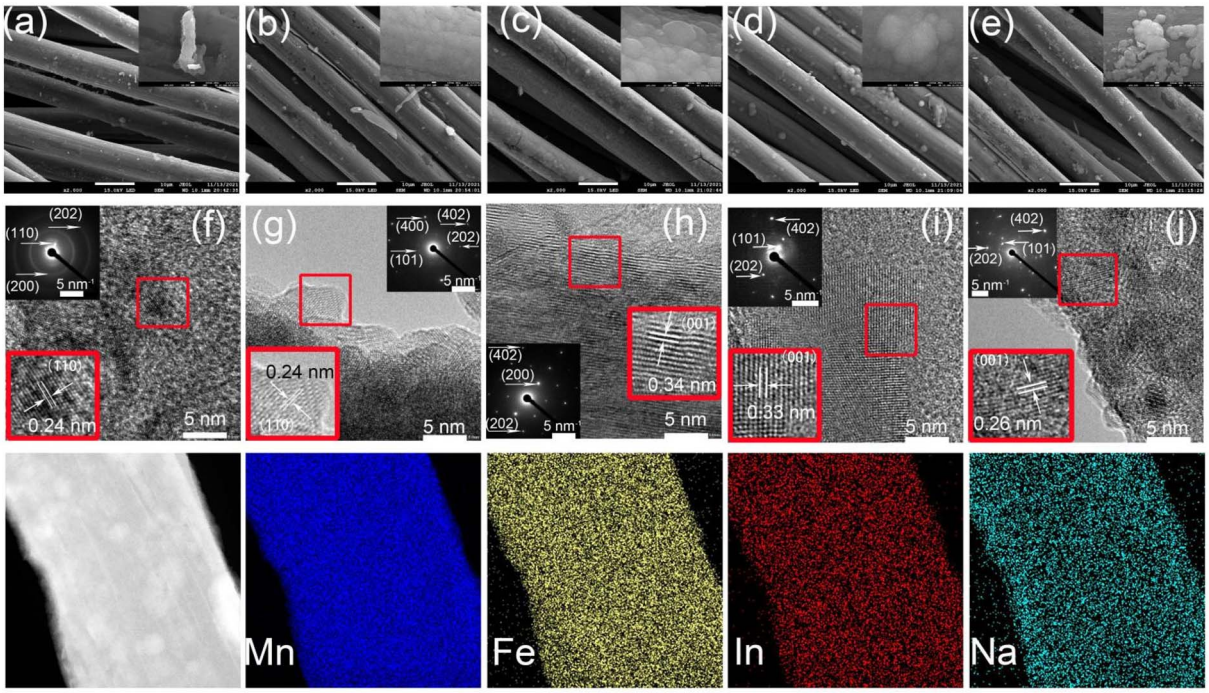

Fig. 2 (a–e) SEM (scale bar: 10 μm) and (f–j) HRTEM images of CC covered with PMO, FeMO, 0.35% InFeMO, 0.7% InFeMO and 1.4% InFeMO, respectively. Bottom: elemental mapping images of Mn, Fe, In and Na with the corresponding TEM image.

Published on 24 Aralk 2022. Downloaded on 9.07.2024 15:25:36.

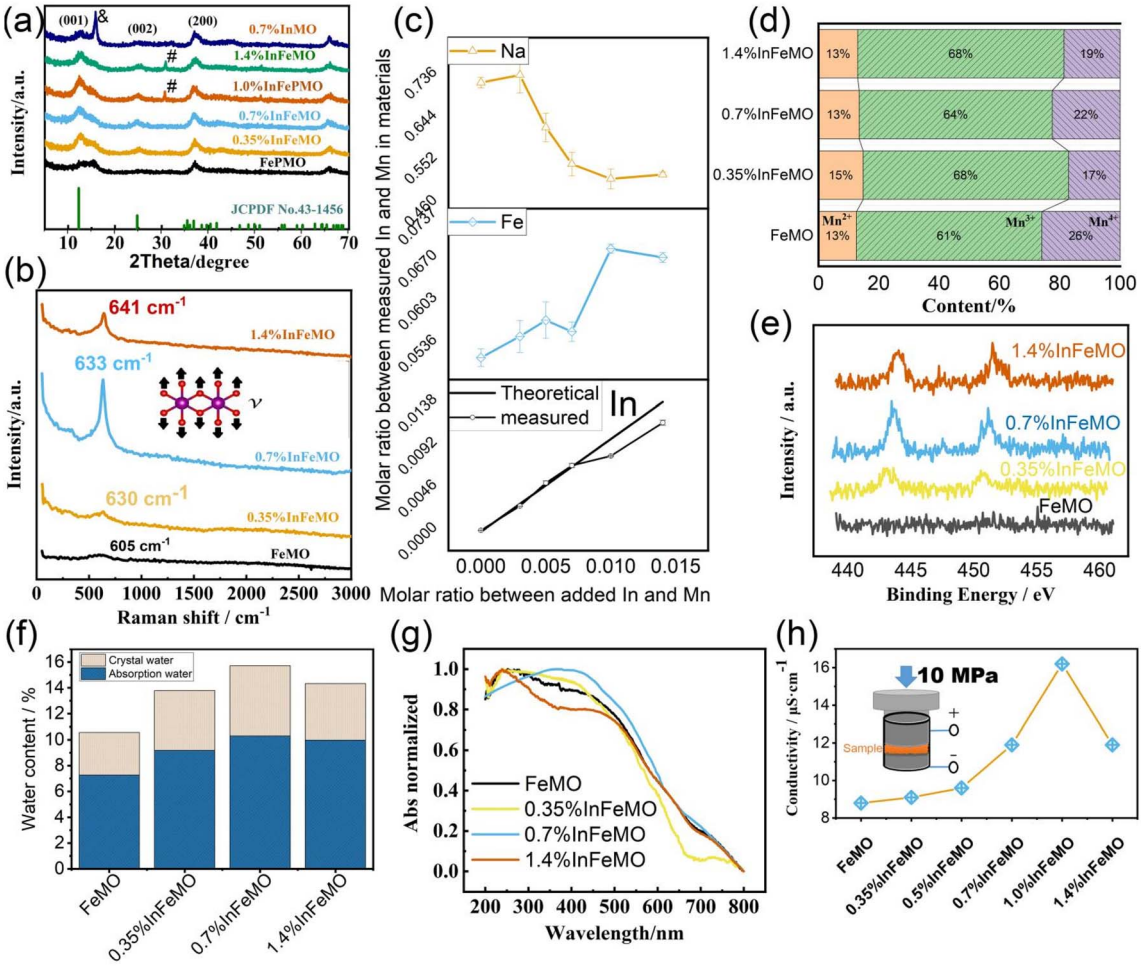

Fig. 3 (a) XRD patterns and (b) Raman spectra of PMO, FeMO, 0.35% InFeMO, 0.7% InFeMO and 1.4% InFeMO. The peaks marked with # and & can be indexed to In_2O_3 and $InMnO_3$, respectively. (c) ICP-MS analysis of the elemental concentration in the solid samples varying with the molar ratio of the In added. (d) The relative content of Mn^{2+}, Mn^{3+} and Mn^{4+} in the samples calculated from the corresponding XPS spectral fitting. High-resolution XPS spectra of (e) In 2p of FeMO, 0.35% InFeMO, 0.7% InFeMO and 1.4% InFeMO. (f) Water in the materials calculated from the TGA curves. (g) Absorbance spectra and (h) electron conductivity of FeMO, 0.35% InFeMO, 0.7% InFeMO and 1.4% InFeMO.

salts.[56–58] This explains why compared to the samples with 5% Fe added, the small amount of Fe in PMO cannot be clearly observed in the measurements, but is still detected in the EDS mapping (Fig. S2a†). The concentration of In increases linearly upon increasing the In ratio when the In/Mn ratio is less than 0.7%. However, the In/Mn ratio is lower than the theoretical ratio calculated from the reactant composition when the In/Mn ratio is higher than 0.7%. This indicates the In cannot be introduced into the materials as designed in reactant composition. This is consistent with the impurity observed in the XRD data. Moreover, the concentration of Fe and Na is also influenced by the In doping. The concentration of Na decreased more than 20%, while the In substituted 1% Mn. This should be attributed to the introduction of In decreasing the binding energy between Na and the δ-MnO_2 facet. This was further confirmed by theoretical studies. The valence states of Mn were identified by fitting the corresponding X-ray photoelectron spectroscopy (XPS) data of the Mn 2p orbitals (Fig. S3†). The relative percentage of all the valence states of Mn changes negligibly as the content of the In dopant increases (Fig. 3(d)). This means that a low amount of In doping will not change the relative percentage of all valence states of Mn, and will maintain the structure of the original δ-MnO_2. The binding energy difference (ΔE_s) between the two Mn 3s peaks can be used to evaluate the average oxidation state.[59] As shown in Fig. S4,† ΔE_s is the same for all the samples. This also demonstrates that the average oxidation state is hardly influenced by the In doping. The XPS spectra of In 2p and Fe 2p are presented in Fig. 3(e) and S5,† respectively. The intensity of the peaks enhanced with the increase in the In dopant, indicating the growing concentration of In in the corresponding solid materials. Another important factor in pseudocapacitive materials is the oxygen vacancy density (OVD). Usually, a higher OVD is favourable for enhancing capacity.[52] The O 1s spectra of the samples are presented in Fig. S6,† which can be deconvoluted into three components at ~529.8, 531.2, and 532.8 eV, denoted as peak1, peak2, and peak3, and ascribed to lattice oxygen, oxygen vacancies, and surface adsorbed oxygen, respectively.[52,60]

 This journal is © The Royal Society of Chemistry 2023

Published on 24 Aralk 2022. Downloaded on 9.07.2024 15:25:36.

Obviously, the introduction of In to the materials increases the OVD due to the enlarged area of peak2 (see Table S1†).

After confirmation that the δ-MnO_2 was birnessite Na_x-$MnO_2 \cdot yH_2O$, to gain more structural information of the material, birnessite $Na_xMnO_2 \cdot yH_2O$ was synthesized *via* a solution method to prepare enough material to carry out some tests that cannot be conducted on CC. In a previous study, it was found that water, especially the crystal water within $Na_xMnO_2 \cdot yH_2O$, can influence its capacitance.[61–63] Thermogravimetric analysis (TGA) results (TG curves are presented in Fig. S7†) of the materials with different dopant composition are presented in Fig. 3(f), wherein it can be observed that 0.7% InFeMO has the highest water content. However, the addition of more In dopant does not increase the amount of water present in the related materials. This should also be attributed to the formation of In_2O_3 as an impurity. It is believed that more crystal water is beneficial for enlarging the interlayer space of birnessite and facilitating ion transport.[62] The water within the interlayer can improve cation transfer from the bulk electrolyte to the particles.[64] The band gap was tested by recording the absorption spectra of the solid materials. No obvious differences can be observed in Fig. 3(g), indicating that In doping does not change the band gap of birnessite. To precisely estimate the conductivity of the materials, solid samples with the same weight were sandwiched between two stainless steel disks in a special plastic chamber, as shown in the inset of Fig. 3(h). The electron conductivity of δ-MnO_2 went from $\sim 10^{-6}$ to 10^{-5} S cm^{-1} when the In dopant concentration increased from 0.0 mol% to 0.7 mol%. This proves that the introduction of In is an effective way (less than 1 mol%) to enhance the conductivity of birnessite $Na_xMnO_2 \cdot yH_2O$. Unfortunately, more In doping leads to a decline in conductivity due to the formation of an impurity phase. This also indicates that developing new methods in future work to increase the In doping concentration in δ-MnO_2 crystals is promising.

To estimate the electrochemical properties of the PMO, FeMO, 0.35% InFeMO, 0.7% InFeMO and 1.4% InFeMO electrodes, a three-electrode system and 1 M Na_2SO_4 as the electrolyte were used. The galvanostatic charge–discharge (GCD) curves of the PMO, FeMO, 0.35% InFeMO, 0.7% InFeMO and 1.4% InFeMO electrodes with a mass loading of 0.5 mg cm^{-2} at a current density of 10 mA g^{-1} are presented in Fig. 4(a). Obviously, 0.7% InFeMO shows the longest discharge time and the highest specific capacitance. The specific capacitances of the PMO, FeMO, 0.35% InFeMO, 0.7% InFeMO and 1.4% InFeMO electrodes at different current densities of 0–50 mA g^{-1} were calculated according to the GCD curves (see Fig. 4(b) and S8†). The sample doped with 0.7 mol% In shows the best performance at all current densities applied. Thus, we focused on the doped material with this composition. Fig. 4(c) shows the evolution of the capacitance of PMO, FeMO and 0.7% InFeMO along with the increase in the current density when their active mass loading was 0.15 mg cm^{-2}. 0.7% InFeMO shows the highest capacitance at all current densities, with 1302 F g^{-1} specific capacitance, which is 95% of the TL, attained at 0.3 A g^{-1}. FeMO has a specific capacitance of only 854 F g^{-1}, which is even lower than that of PMO. Because the mass loading is very low, the influence of electron conductivity is negligible. The lower capacitance of FeMO might arise from the lower diffusion-controlled capacitive contribution. However, when the mass loading is higher than 0.5 mg cm^{-2}, the poor conductivity of PMO starts to hinder the specific capacitance (Fig. 4(d)). In contrast to PMO, FeMO and 0.7% InFeMO have high gravimetric and areal capacitance due to their high conductivity, with their areal capacities at different current densities shown in Fig. 4(e). The areal capacitances of 0.7% InFeMO at 0.3 A g^{-1} and 1.0 A g^{-1} almost overlap when the mass loading increases from 0.15 mg cm^{-2} to 11 mg cm^{-2}. However, the difference in the capacitance of FeMO and PMO at 0.3 A g^{-1} and 1.0 A g^{-1} increases with increasing mass loading. This means 0.7% InFeMO has better rate capability, which should be attributed to its higher conductivity.

To analyze the charge storage mechanism of the materials, surface capacitive or diffusion contributions to the energy storage were calculated using Dunn's test.[65] First, the CV curves of the active materials were measured at various scan rates (see Fig. 4(f) and S9†), then the current density of each curve was described as follows:

$$i = k_1 v + k_2 v^{0.5} \tag{1}$$

where v is the scan rate (V s^{-1}). k_1 and k_2 can be solved according to the CV curves obtained at different scan rates. For any CV curve at specific scan rate, $k_1 v$ is the capacitive contribution, while $k_2 v^{0.5}$ is the diffusion contribution. Fig. 4(g) shows the CV curve with the brown region representing the surface capacitance at a scan rate of 100 mV s^{-1}. Accordingly, the proportions of capacitive or diffusion contributions at different scan rates are given in Fig. 4(h). For all of the materials, the ratio of the surface capacitive charge increases with increasing scan rate. Interestingly, FeMO exhibits the lowest ion diffusion contribution to the capacitance, which explains its inferior capacitance at even very low mass loading. The diffusive contribution of the capacitance of 0.7% InFeMO is 60–65% when the scan rate increases from 1 to 10 mV s^{-1}. It remains at around 35% at 10 mV s^{-1}, while that of PMO and FeMO drops lower than 10%. Thus, we attribute the better charge capacitive performance of 0.7% InFeMO to its higher conductivity and lower ion diffusion resistivity, which partially originates from the crystal water.[62,63] Besides this, the nanoflower structure of 0.7% InFeMO with a porous morphology can also facilitate ion diffusion.[48] To confirm the universal effectiveness of In doping, samples prepared from solution were used to fabricate electrodes by pasting them on nickel foam. The 0.7% InFeMO electrode also exhibits superior performance to the FeMO electrode (Fig. S10†).

Lower mass loading means less dead mass on the electrode and the active materials can function completely. Long-term cycling performances of the PMO, FeMO and 0.7% InFeMO electrodes at a low mass loading (0.5 mg cm^{-2}) were evaluated in 1 M Na_2SO_4 aqueous solution. The capacitance of PMO degrades quickly after only 3k charge/discharge cycles, whereas that of FeMO drops to lower than 80% of its original capacitance after 10k cycles and the degradation is even accelerated towards

Published on 24 Aralk 2022. Downloaded on 9.07.2024 15:25:36.

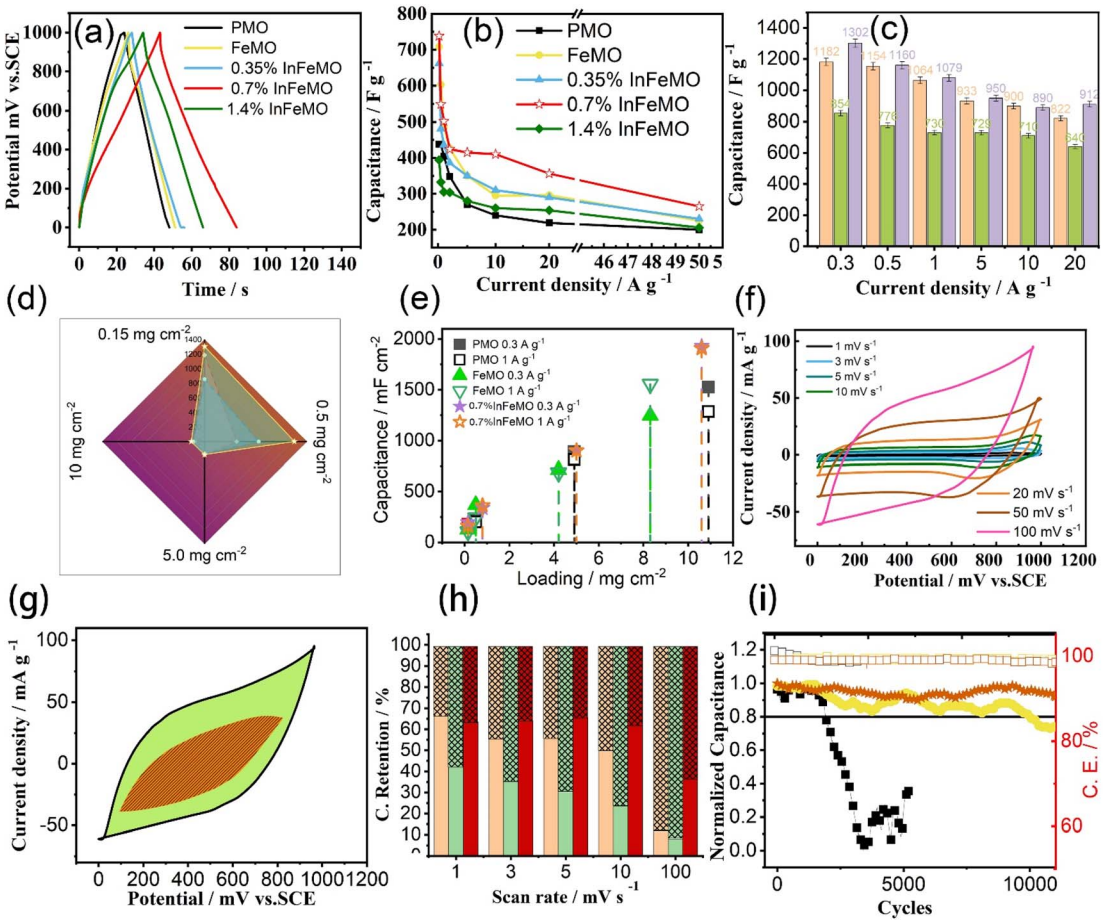

Fig. 4 (a) Charge/discharge curves of the PMO, FeMO, 0.35% InFeMO, 0.7% InFeMO and 1.4% InFeMO electrodes at a current density of 10 mA g^{-1}. (b) The specific capacitances of the PMO, FeMO, 0.35% InFeMO, 0.7% InFeMO and 1.4% InFeMO electrodes at different current densities. The mass loading was 0.5 mg cm^{-2} for all electrodes in both (a) and (b). The limits of the experimental capacitance of the PMO (wheat), FeMO (green) and 0.7% InFeMO (purple) are shown in (c). (d) The influence of mass loading on the specific capacitances of the PMO (red shading), FeMO (blue shading) and 0.7% InFeMO (yellow shading, current density of 0.3 mA cm^{-2} for all). (e) The areal capacitances of the PMO, FeMO and 0.7% InFeMO electrodes with a mass loading from 0.15 to 11 mg cm^{-2} at different current densities. (f) CV curves of the InFeMO electrodes at various scan rates. (g) CV curve of the InFeMO electrode with the shadowed area representing the surface capacitive contribution. (h) The diffusion-controlled (colored only) and capacitive charge (shadowed) at different scan rates for the PMO (wheat), FeMO (green) and 0.7% InFeMO (red) electrodes. (i) Cycling performances of the PMO (black), FeMO (yellow) and InFeMO (red) electrodes in 1 M Na_2SO_4 at a mass loading of 0.5 mg cm^{-2}.

the end of the measurements. Meanwhile, 0.7% InFeMO shows no capacitive degradation after 10k cycles. The 0.7% InFeMO material has a greater amount of interlayer water than the other materials, which has been proved to be effective for preventing structural changes.[66] Thus, the interlayer water also boosts the cycling stability here. To confirm the positive influence of In doping on the morphology during charge/discharge cycling, scanning electron microscopy (SEM) was conducted to study the morphology changes of the carbon cloth covered by PMO, FeMO and 0.7% InFeMO, respectively. In Fig. S11,† the active material on carbon fibers peels off and seems to expand after cycling. For the material covered by FeMO, many cracks are observed on the fibers. Surprisingly, the active material of 0.7% InFeMO still compactly covers the carbon fibers, with a negligible change in its morphology. Only some white solid, which may be Na_2SO_4 from the electrolyte, can be observed on the surface of the material. This is solid proof that In doping prevents structural changes of the active materials effectively.

An asymmetric supercapacitor (ASC) device was assembled with 0.7% InFeMO as a positive electrode and commercially available AC as the negative electrode (0.7% InFeMO//AC). 1 M Na_2SO_4 as the electrolyte was applied in the testing for each material in both a three electrode system and an ASC. The CV curves of the AC electrode and 0.7% InFeMO electrode across potential windows of −1.0–0.0 V and 0.0–1.4 V, respectively, are presented in Fig. 5(a). The GCD curve of the AC electrode is shown in Fig. S12.† The specific capacitance of the AC electrode with such high mass loading is only 79 F g^{-1} at a current intensity of 1 A g^{-1}. To achieve good electrochemical performance of the ASC, the ratio between the capacitance of the 0.7% InFeMO and AC electrodes was around 1.5 at a discharge current density of 10 mA cm^{-2}.[67] Fig. 5(b) shows the CV curves

 This journal is © The Royal Society of Chemistry 2023

Published on 24 Aralk 2022. Downloaded on 9.07.2024 15:25:36.

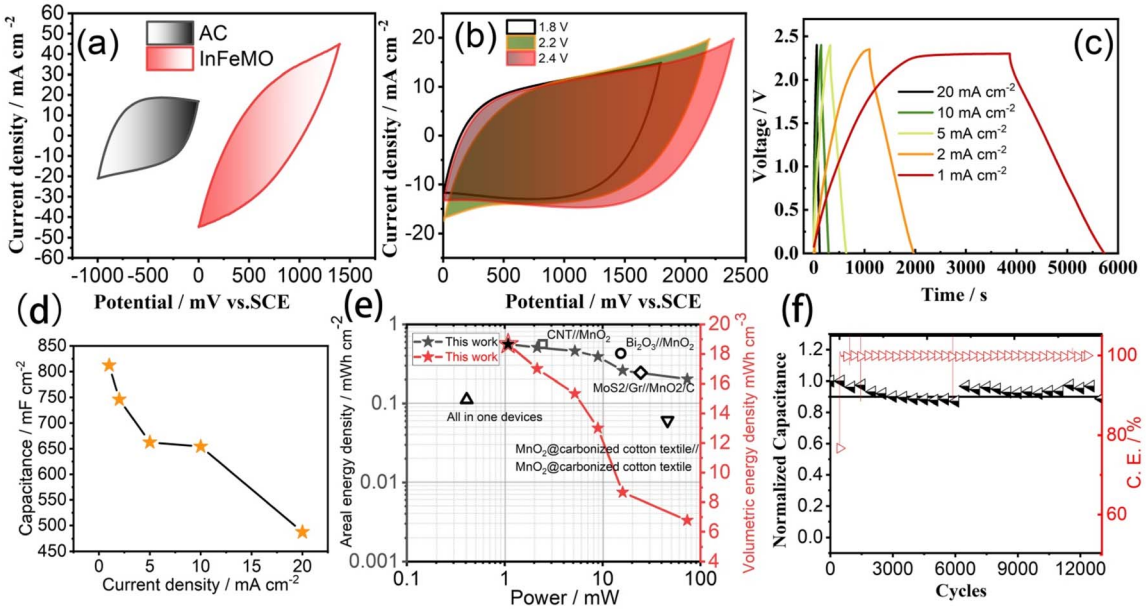

Fig. 5 (a) CV curves of the AC and 0.7% InFeMO electrodes in separate potential windows at a scan rate of 20 mV s^{-1}. (b) CV curves of the 0.7% InFeMO//AC ASC in different voltage windows at a scan rate of 20 mV s^{-1}. (c) GCD curves of the 0.7% InFeMO//AC ASC at a current density from 1 to 20 mA cm^{-2}. (d) The areal capacitance of 0.7% InFeMO//AC ASC at different current densities. (e) Ragone plots. (f) Cycling stability of the ASC in 1 M Na_2SO_4 aqueous solution at 20 mA cm^{-2}.

of the 0.7% InFeMO//AC ASC device operated across potential windows of 0–1.8 V, 0–2.2 V, and 0–2.4 V. A wider operating voltage window is beneficial for the areal energy density according to calculations. Here, the aqueous 0.7% InFeMO//AC ASC device operated across the 0–2.4 V operating voltage window is in the class of high-voltage aqueous ASCs.[68] The CV curves of the 0.7% InFeMO//AC ASC at a scan rate of 20 mV s^{-1} are near rectangular, which indicates that the device shows ideal capacitive behavior. The GCD curves of the 0.7% InFeMO//AC ASC device in Fig. 5(c) show its charge/discharge behavior. As long as the charging current density is higher than 2 mA cm^{-2}, the device operates well within the 0–2.4 V voltage window. Even when the current density decreases to 1 mA cm^{-2}, 2.35 V is achievable. An excellent areal capacitance 820 mF cm^{-2} at a current density of 1 mA cm^{-2} was achieved, as shown in Fig. 5(d). The 0.7% InFeMO//AC ASC device also shows rapid charge/discharge capability of 79% capacitance retention at 10 mA cm^{-2}. The energy density and power density of the 0.7% InFeMO//AC ASC device were calculated. Ragone plots of the 0.7% InFeMO//AC ASC device and some high performance supercapacitors are presented in Fig. 5(e). A high areal energy density of 0.55 mW h cm^{-2} and a volumetric energy density of 18.7 mW h cm^{-3} at an areal power density of 1.0 mW cm^{-2} were obtained. The areal energy density and volumetric energy density retained 0.39 mW h cm^{-2} and 13.0 mW h cm^{-3}, respectively, at an areal power density of ~10 mW cm^{-2}. This outstanding device performance was achieved by using a regular AC and no ancillary nanotechnologies. Thus, this should be only attributed to the intrinsic high capacitance of the cathode material 0.7% InFeMO. For comparison, some of the results reported in similar cutting-edge research studies are given in Table S2.†

In previous research, the capacitance retention decreased with an increase in mass loading.[23] Therefore, we evaluated the capacitance retention of the 0.7% InFeMO//AC ASC device at a high mass loading (45 mg cm^{-2} on both electrodes) and a current density of 20 mA cm^{-2} (444 mA g^{-1}) for deep cycling. The initial capacitance was 483.3 mF cm^{-2}. After 13 000 charge/discharge cycles, 435 mF cm^{-2} was retained, representing 90% capacitance retention (Fig. 5(f)).

In order to understand the mechanism underlying the outstanding performance of In-doped materials, more experimental and theoretical investigations were conducted. As discussed earlier, the diffusion charge contributes greatly to the total capacitance of the materials, especially 0.7% InFeMO. We conducted galvanostatic intermittent titration technique (GITT) measurements to estimate the diffusion coefficient of sodium ions (D_{Na^+}) in the electrode materials (Fig. 6(a–c)). The D_{Na^+} values of the electrode materials are in the range of 10^{-14}–10^{-9} cm^2 s^{-1}. In the voltage range of 1.0–1.5 V, FeMO and 0.7% InFeMO exhibit higher D_{Na^+} (~10^{-11} cm^2 s^{-1}) values than PMO (~10^{-12} cm^2 s^{-1}) during the charge process. At the end of the charge process, the D_{Na^+} values of all the materials fell to 10^{-14} cm^2 s^{-1}. In the discharge process, PMO shows the highest D_{Na^+} value (10^{-9} cm^2 s^{-1}) while FeMO and 0.7% InFeMO present moderate D_{Na^+} (10^{-11} cm^2 s^{-1}) values. FeMO shows similar D_{Na^+} values in both charge/discharge processes. To understand the effect of the dopants on the D_{Na^+}, the diffusion barrier energy (DBE) of the materials was calculated using density functional theory (DFT). Fig. 6(d) shows the sodium ion diffusion during the charge/discharge process. In both diffusion directions,

Published on 24 Aralk 2022. Downloaded on 9.07.2024 15:25:36.

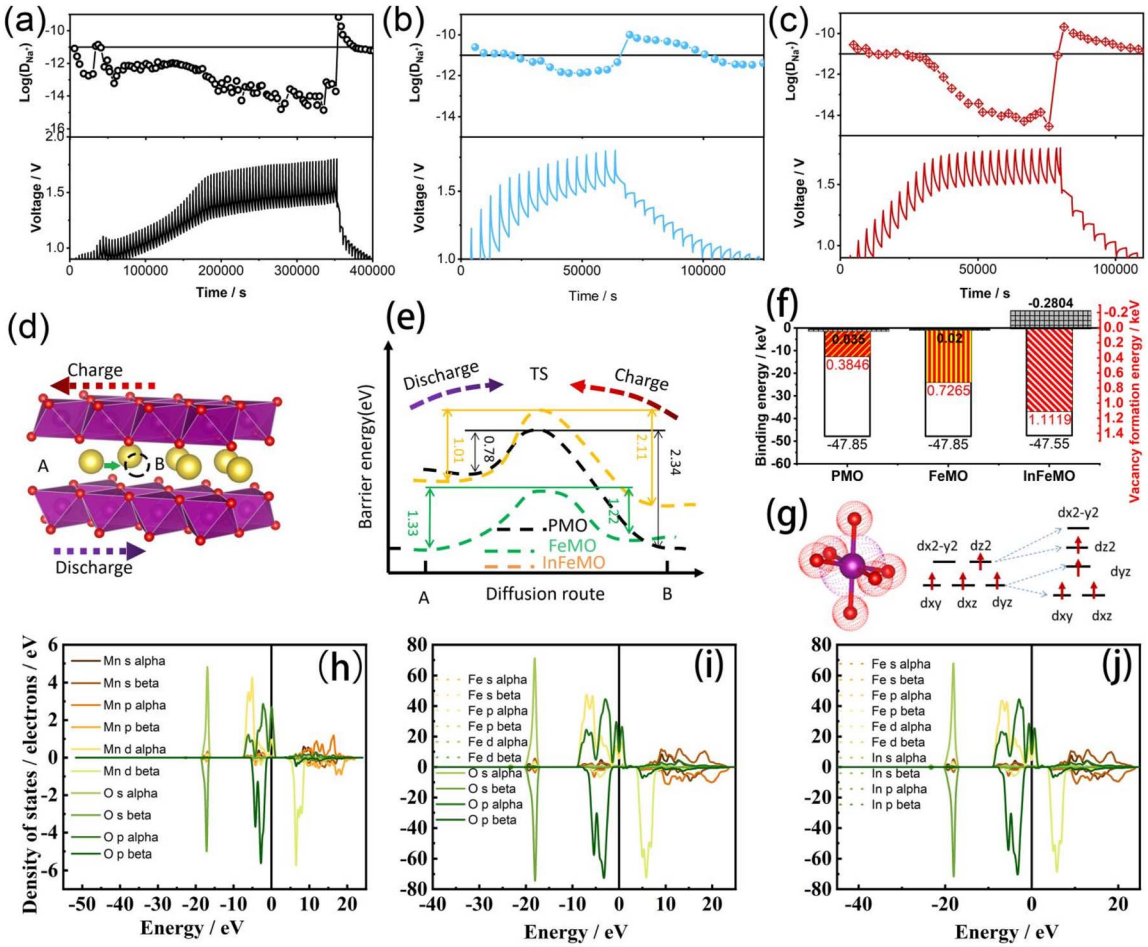

Fig. 6 The charge/discharge GITT profiles of (a) PMO, (b) FeMO and (c) 0.7% InFeMO and the corresponding diffusive coefficients ($cm^2\ s^{-1}$) are presented. (d) Schematic illustration of sodium ion diffusion during the charge/discharge process. (e) The diffusive barrier of sodium ions in PMO, FeMO and InFeMO. (f) Binding energy (blank) of PMO, FeMO and InFeMO. Vacancy formation energy of Mn (red shading) and Na (gray shading). (g) The octahedral structure of [MnO_6] and the electron occupation of the crystal field splitting d orbitals of [$Mn^{3+}O_6$] for PMO (left) and doped δ-MnO_2 (right). (h–j) DOS of PMO, FeMO and InFeMO, respectively. The related atomic orbital contributions at different energy levels are presented in different colors.

FeMO has the same DBE, which explains its similar D_{Na^+} values in both charge/discharge processes in the experiments. In the discharge process, the DBE of PMO is 0.78 eV, which is the lowest value among the materials, and is in agreement with the highest D_{Na^+} value of PMO in the discharge process. In contrast, the DBE of PMO is 2.34 eV, corresponding to it exhibiting the lowest D_{Na^+} value in the charge process. The DBEs of all the electrode materials explain the D_{Na^+} values in the charge/discharge process well.

To gain more understanding of the excellent cycling performance of In-doped materials, detailed first-principles calculations were conducted. The total binding energies (E_b) of PMO, FeMO, and In–Fe co-doped MnO_2 (InFeMO) are given in Fig. 6(f). The E_b value of PMO and FeMO is −47.85 eV, while the E_b value of InFeMO is −47.55 eV. There is no distinct difference in E_b in all cases. The E_b value of InFeMO is only slightly lower than that of the materials. Usually, a more negative E_b value indicates higher thermodynamic stability. The E_b results even contradicted the experimental results in that the In-doped materials have low Na concentration. E_b is a measure of all the interactions between the elements, including Mn, Na, O, In and Fe, in the materials. Thus, the vacancy formation energies (E_{vf}) of the electrode materials were calculated to analyse the interaction between a specific atom and a material. The larger the E_{vf} value, the stronger connection between the corresponding atom and the δ-MnO_2 slabs, and the higher the confinement effect on the Mn dissolution from the materials. The E_{vf} value of FeMO is double that of PMO, while the E_{vf} value of InFeMO increases to 1.1119 keV, which is 3 times higher than that of PMO, which explains the outstanding cycling stability of InFeMO. The relative lower E_b value of InFeMO arises from its low E_{vf} value of Na. The low E_{vf} value of Na in InFeMO indicates that there is a weak interaction between Na and the δ-MnO_2 slabs, which facilitates Na ion diffusion. It explains the decline in Na concentration of the In-doped materials. The distortion of the crystal structure during the charge/discharge process, also known as Jahn–Teller distortion, is another main reason for the Mn dissolution from the δ-MnO_2 slabs. The typical crystal field

 This journal is © The Royal Society of Chemistry 2023

Published on 24 Aralk 2022. Downloaded on 9.07.2024 15:25:36.

splitting of d orbitals in an octahedral environment is shown in Fig. 6(g), left). The single electron occupancy in the doubly degenerate e_g level causes Jahn–Teller distortion. Jahn–Teller distortion can be hindered by further splitting the e_g level, according to the description in Fig. 6(g), right).[47] We believe that the introduction of Fe and In leads to the level splitting of e_g. In order to confirm this speculation, the density of states (DOS) of PMO, FeMO and InFeMO were calculated and the results are presented in Fig. 6(h–j). The valence bands of the materials are composed of d orbitals from Mn and p orbitals from O. At the Fermi level, a sharp single peak is observed in the DOS of PMO. In the case of FeMO, the peak is split into two peaks. This should be attributed to the level splitting of e_g due to the composition of the valence bands. Fe as a dopant decreases the band gap, which is in agreement with the results of a previous study.[39] The introduction of In maintains the level splitting of e_g and the narrowed band gap.

3 Experimental

3.1. Preparation of δ-MnO_2

Electrochemical deposition was applied to coat carbon cloth (HCP330N, Kelude Co.) with δ-MnO_2. The carbon cloth was annealed at 400 °C for 2 h to enhance its hydrophilicity. Manganese acetate hydrate ($MnAc_2 \cdot 4H_2O$, 99%), iron chloride ($FeCl_3$, 99%) and indium sulfate ($In_2(SO_4)_3$, 99.99%) were dissolved in water to prepare an aqueous solution (about 0.1 M, based on total metal ions). For the iron-doped sample, 5 mol% $FeCl_3$ of the total metal ions and 95 mol% $MnAc_2$ were dissolved in water. For the iron- and indium-doped samples, x mol% $In_2(SO_4)_3$, 5.0 mol% $FeCl_3$ and $(95.0 - x)$ mol% $MnAc_2$ were added to the water. x is a number from 0.0 to 1.4. The samples prepared from the solutions above were denoted as pure δ-MnO_2 (PMO), Fe-doped δ-MnO_2 (FeMO) and x% InFeMO. For the electrochemical deposition, a piece of carbon cloth (3×3 cm^2) was used as the working electrode, while a saturated calomel electrode (SCE) and a Pt plate were used as reference and counter electrodes, respectively, and the as-prepared solution as the electrolyte. 900 mV *vs.* SCE was applied for 120–3600 s to obtain δ-MnO_2 covered carbon cloth with a mass loading varying from 0.2 to 12 mg cm^{-2}. For the δ-MnO_2 prepared *via* a hydrothermal method,[39] manganese chloride ($MnCl_2$, 99%) was used as the manganese source. The other metal sources were the same as used in the electrochemical deposition method. The molar ratios of the related ions were added to water in the same way mentioned above. Under vigorous stirring, 25 mL of a solution with a concentration of 0.5 M based on the total metal ion content was added to 50 mL of a 5 M sodium hydroxide solution, and then 50 mL of potassium permanganate was dropped into the resulting slurry. The mixture was stirred at room temperature for 30 min to form a tan suspension, which was then aged for 24 h before being transferred to stainless steel hydrothermal kettles. After heating at 150 °C for 12 h and cooling to room temperature, the solid was collected by centrifugation. The solid was washed with water until the pH reached 7. The samples were obtained by drying the solids and annealing at 400 °C for 2 h.

3.2. Materials characterization

SEM images were obtained on a JSM-7800F instrument at an acceleration voltage of 15 kV. TEM images and energy-dispersive X-ray (EDX) mapping spectra were recorded on a JEM-2800F instrument at an acceleration voltage of 300 kV. XPS were recorded on a Thermo Scientific ESCALAB 250Xi spectrometer using an aluminum anode (Al 1486.6 eV) X-ray source. XRD data were obtained using a Rigaku Ultima IV diffractometer equipped with a Cu K_α radiation ($\lambda = 1.54$ Å) source. Raman spectra were acquired on a Renishaw inVia Reflex spectrometer using 514 nm laser excitation. TGA measurements were conducted on a SDT Q600 instrument under atmospheric conditions. Inductively coupled plasma mass spectrometry (ICP-MS) data were obtained on an Agilent 7700X spectrometer. To evaluate the conductivity of the materials, a specific voltage was applied between the disks, and the current was recorded, while 10 MPa pressure was applied for all samples. After measurement of the thickness of the sample disks, the resistance and the conductivity of the materials were calculated using Ohm's law.

3.3. Electrochemical measurements and quantification

Cyclic voltammetry (CV) curves, GCD curves and impedance spectra (EIS) of the samples were measured on an electrochemical workstation (Tianjin Lanlike/LK 2010). A three-electrode system was used to test the electrochemical performance of the active materials using a saturated calomel electrode (SCE) and Pt sheet as reference and counter electrodes, respectively. 1.0 mol L^{-1} Na_2SO_4 solution was used as the electrolyte. The CV curves has a sweep rate range of 1–100 mV s^{-1}. A liquid NASC device was assembled using δ-MnO_2/CC and active carbon/nickel foam as the positive and negative electrodes, respectively. δ-MnO_2/CC was used as the binder-free electrode, while the anode was nickel foam coated with carbon slurry containing active carbon (from Xianfeng Nano Technology Co.), carbon black and chlorinated rubber in a weight ratio of 8 : 1 : 1. Asymmetric supercapacitor devices with two electrode configurations were tested in the same electrolyte as the three-electrode system. For the high mass loading device, the total mass loading of active material in both electrodes was 45 mg cm^{-2}. Specific capacitance (F g^{-1}) of electrode materials as well as the device were calculated from the GCD curves using the following equation:

$$C = \frac{I\Delta t}{A\Delta V} \tag{2}$$

where A is the area of the electrode (cm^2), I is the current (A), Δt denotes the discharge time (s), and ΔV is the potential or voltage window (V). The areal energy density (E, W h cm^{-2}) and specific power (P, W cm^{-2}) of the device were obtained from the following equations:

$$E = \frac{C\Delta V^2}{2 \times 3.6} \tag{3}$$

$$P = \frac{3600 \times E}{\Delta t} \tag{4}$$

Published on 24 Aralk 2022. Downloaded on 9.07.2024 15:25:36.

Long term charge–discharge cycling tests and GITT measurements were conducted on a Neware battery test system. The diffusion coefficient of Na^+ was obtained using eqn (5):

$$D_{Na^+} = \frac{4}{\pi\tau}\left(\frac{m}{\rho S}\right)^2\left(\frac{\Delta E_s}{\Delta E_\tau}\right)^2 \quad (5)$$

where τ is the constant current pulse time, m and ρ are the mass and calculated density of $Na_xMnO_2 \cdot yH_2O$, respectively, S is the electrode–electrolyte interface area, ΔE_s is the steady-state voltage change related to the current pulse, and ΔE_τ is the voltage change during the constant current pulse.

3.4. Theoretical calculations

The CASTEP program was used to carry out the theoretical calculations.[69] The Perdew–Burke–Ernzerhof for solid (PBESol) exchange–correlation functions of the generalized gradient approximation (GGA) was used for the treatment of the electronic-exchange–correlation potential. The DFT+U approach was used to calculate the total energy and density of states of the electrons. The convergence criteria of the maximum energy change, the maximum displacement, and the maximum stress were set as 2×10^{-5} eV per atom, 2×10^{-3} Å, and 0.1 GPa, respectively. Spin polarization was considered in all calculations. For $NaMnO_2$ unit cell optimization, $1 \times 1 \times 1$ k-point samplings were used. Based on the optimized $NaMnO_2$ unit cell (ICSD deposition number: 1598711), it was expanded to a $4 \times 5 \times 1$ supercell, and one Mn atom was substituted with Mx (Fe or In) to obtain the doped supercells. The E_b values were defined as follows:

$$E_b = E_{cell} - E_{Mn} - E_O - E_{Na} - E_D \quad (6)$$

where E_{cell} is the total energy of the δ-MnO_2 supercell, and E_{Mn}, E_O, E_{Na} and E_x are the energies of Mn, O, Na and D (Fe or In), respectively. The E_{vf} values were calculated using the following equation:

$$E_{vf} = E_d - E_p + \sum kP_i \quad (7)$$

where E_d and E_p are the total energies of defective (with one Mn or eight Na vacancies) and perfect birnessite δ-MnO_2 supercells, respectively, P_i is the potential of an atom replaced by a vacancy, and k is the number of vacancies.

4 Conclusions

In summary, we demonstrated that the introduction of In into birnessite δ-MnO_2 can significantly influence its intrinsic properties. In as a dopant enhances the conductivity of δ-MnO_2 from $\sim 10^{-6}$ to 10^{-5} S cm^{-1} and increases the amount of crystal water present between the slabs of birnessite. These properties boost the capacitance of birnessite on electrodes with both low and high mass loading, due to the electron transport and sodium ion diffusion in δ-MnO_2. Using commercial AC as a negative electrode, a NASC with commercial-level mass-loading of δ-MnO_2 was fabricated using no ancillary nanotechnologies. This NASC shows a high areal energy density of 0.55 mW h cm^{-2} and a volumetric energy density of 18.7 mW h cm^{-3} at an areal power density of 1.0 mW cm^{-2}. The device with a high mass loading presents 90% capacitance retention after 13 000 charge/discharge cycles. DFT calculations confirm that the In dopant strengthens the layered structure *via* a suppressed Jahn–Teller effect and facilitates sodium ion diffusion. Because of the fundamental role played by δ-MnO_2 in related devices, this study details the preparation of a novel In-doped δ-MnO_2 materials and gives new opportunities for constructing high-performance supercapacitors and water-purification devices. In the future, this material can be incorporated with other nano technologies to fabricate more advanced devices. Last but not least, this study presented a new way to introduce dopant elements that cannot be introduced directly into the crystal structure of δ-MnO_2.

Author contributions

B. L. and Y. C. contributed equally to this paper. Y. C. and J. H. conceived the ideas. B. L., Y. C., L. Z. and J. H. designed the experiments, fabricated the samples, measured the electrochemical performance and wrote the paper. J. H. supervised the project, analyzed the data and revised the paper. B. X., Y. S., L. Z., H. Z. and Y. W. helped with the electrochemical performance measurements and analysis. P. L. and J. H. contributed to the theoretical calculations.

Conflicts of interest

There are no conflicts to declare.

Acknowledgements

The authors acknowledge the financial support from the National Natural Science Foundation of China (12064050); the Key Project of R&D Plan of Yunnan Province (202203AC100004); and the Major Project of Science and Technology of Yunnan Province under Grant (202002AE090010).

Notes and references

1 B. Bounor, B. Asbani, C. Douard, F. Favier, T. Brousse and C. Lethien, *Energy Storage Mater.*, 2021, **38**, 520.
2 R. Ma, Z. Chen, D. Zhao, X. Zhang, J. Zhuo, Y. Yin, X. Wang, G. Yang and F. Yi, *J. Mater. Chem. A*, 2021, **9**, 11501.
3 S. Cheng, Z. Dai, J. Fu, P. Cui, K. Wei, Y. Zhang, Y. Wu, Y. Liu, Z. Sun, Z. Shao, X. Cui, Q. Su and E. Xie, *J. Mater. Chem. A*, 2021, **9**, 622.
4 Q. Wu, T. He, Y. Zhang, J. Zhang, Z. Wang, Y. Liu, L. Zhao, Y. Wu and F. Ran, *J. Mater. Chem. A*, 2021, **9**, 24094.
5 P. Wang, X. Ding, R. Zhe, T. Zhu, C. Qing, Y. Liu and H.-E. Wang, *Nanomaterials*, 2022, **12**, 1094.
6 L. Zheng, Y. Zhao, P. Xu, Y. Pan, P. Yang, H.-E. Wang, N. Li, X. Shi and H. Zheng, *J. Alloys Compd.*, 2022, **911**, 165115.
7 J. Ren, M. Shen, Z. Li, C. Yang, Y. Liang, H.-E. Wang, J. Li, N. Li and D. Qian, *J. Power Sources*, 2021, **501**, 230003.

 This journal is © The Royal Society of Chemistry 2023

Published on 24 Aralk 2022. Downloaded on 9.07.2024 15:25:36.

8 T. Zhu, J. Pan, Z. An, R. Zhe, Q. Ou and H.-E. Wang, *J. Mater. Chem. A*, 2022, **10**, 20375.
9 X. Han, C. Wu, H. Li, Y. Zhang, W. Sun, B. Jia, I. D. Gates, Z.-H. Huang and T. Ma, *Adv. Funct. Mater.*, 2022, **32**, 2113209.
10 G. Liu, Y. Qin, Y. Lyu, M. Chen, P. Qi, Y. Lu, Z. Sheng and Y. Tang, *Chem. Eng. J.*, 2021, **426**, 131248.
11 S. Kumar, G. Saeed, L. Zhu, K. N. Hui, N. H. Kim and J. H. Lee, *Chem. Eng. J.*, 2021, **403**, 126352.
12 J. S. Chen, L. Wei, A. Mahmood, Z. X. Pei, Z. Zhou, X. C. Chen and Y. Chen, *Energy Storage Mater.*, 2020, **25**, 585.
13 C. Miao, C. Zhou, H.-E. Wang, K. Zhu, K. Ye, Q. Wang, J. Yan, D. Cao, N. Li and G. Wang, *J. Power Sources*, 2021, **490**, 229532.
14 P. Xie, W. Yuan, X. B. Liu, Y. M. Peng, Y. H. Yin, Y. S. Li and Z. P. Wu, *Energy Storage Mater.*, 2021, **36**, 56.
15 X. F. Zou, Y. Zhou, Z. P. Wang, S. J. Chen, W. P. Li, B. Xiang, L. K. Xu, S. S. Zhu and J. Hou, *Chem. Eng. J.*, 2018, **350**, 386.
16 H. Mahajan, K. U. Mohanan and S. Cho, *Nano Lett.*, 2022, **22**, 8161.
17 Y. D. Zhang, P. Nie, C. Y. Xu, G. Y. Xu, B. Ding, H. Dou and X. G. Zhang, *Electrochim. Acta*, 2018, **268**, 512.
18 Y. Song, T. Y. Liu, B. Yao, T. Y. Kou, D. Y. Feng, X. X. Liu and Y. Li, *Small*, 2017, **13**, 1700067.
19 Y. Ding, S. Zhang, J. Li, Y. Sun, B. Yin, H. Li, Y. Ma, Z. Wang, H. Ge, D. Su and T. Ma, *Adv. Funct. Mater.*, 2022, **32**, 2210519.
20 M. Chuai, J. Yang, R. Tan, Z. Liu, Y. Yuan, Y. Xu, J. Sun, M. Wang, X. Zheng, N. Chen and W. Chen, *Adv. Mater.*, 2022, **34**, 2203249.
21 H. Liu, X. Liu, S. L. Wang, H. K. Liu and L. Li, *Energy Storage Mater.*, 2020, **28**, 122.
22 Y. Yuan, C. Liu, B. W. Byles, W. Yao, B. Song, M. Cheng, Z. Huang, K. Amine, E. Pomerantseva, R. Shahbazian-Yassar and J. Lu, *Joule*, 2019, **3**, 471.
23 J.-M. Jeong, S. H. Park, H. J. Park, S. B. Jin, S. G. Son, J.-M. Moon, H. Suh and B. G. Choi, *Adv. Funct. Mater.*, 2021, **31**, 2009632.
24 J. Zhang, X. Yang, Y. He, Y. Bai, L. Kang, H. Xu, F. Shi, Z. Lei and Z.-H. Liu, *J. Mater. Chem. A*, 2016, **4**, 9088.
25 B. Yao, S. Chandrasekaran, J. Zhang, W. Xiao, F. Qian, C. Zhu, E. B. Duoss, C. M. Spadaccini, M. A. Worsley and Y. Li, *Joule*, 2019, **3**, 459.
26 X. Y. Lang, A. Hirata, T. Fujita and M. W. Chen, *Nat. Nanotechnol.*, 2011, **6**, 232.
27 Y. Chen, B. Zhao, Y. Yang and A. Cao, *Adv. Energy Mater.*, 2022, **12**, 2201834.
28 S. Dang, Y. X. Wen, T. F. Qin, J. X. Hao, H. Q. Li, J. J. Huang, D. Yan, G. Z. Cao and S. L. Peng, *Chem. Eng. J.*, 2020, **396**, 125342.
29 T. Y. Liu, Z. P. Zhou, Y. C. Guo, D. Guo and G. L. Liu, *Nat. Commun.*, 2019, **10**, 675.
30 H. Y. Wang, C. M. Xu, Y. Q. Chen and Y. Wang, *Energy Storage Mater.*, 2017, **8**, 127.
31 C. J. Chen, Y. Zhang, Y. J. Li, J. Q. Dai, J. W. Song, Y. G. Yao, Y. H. Gong, I. Kierzewski, J. Xie and L. B. Hu, *Energy Environ. Sci.*, 2017, **10**, 538.
32 F. Wang, X. L. Liu, G. G. Duan, H. Q. Yang, J. Y. Cheong, J. Lee, J. Ahn, Q. Zhang, S. J. He, J. Q. Han, Y. Zhao, I. D. Kim and S. H. Jiang, *Small*, 2021, **17**, e2102532.
33 Z. Xiong, Y. Cao, W.-J. Jiang, L. Zu, Q. Liang and D. Li, *Energy Storage Mater.*, 2022, **53**, 444.
34 J. M. Jeong, S. H. Park, H. J. Park, S. B. Jin, S. G. Son, J. M. Moon, H. Suh and B. G. Choi, *Adv. Funct. Mater.*, 2021, **31**, 131248.
35 B. J. Choudhury and V. S. Moholkar, *Ultrason. Sonochem.*, 2022, **82**, 105896.
36 D. Z. Kong, J. S. Luo, Y. L. Wang, W. N. Ren, T. Yu, Y. S. Luo, Y. P. Yang and C. W. Cheng, *Adv. Funct. Mater.*, 2014, **24**, 3815.
37 H. T. Zhu, L. Y. Li, M. J. Shi, P. Xiao, Y. T. Liu and X. B. Yan, *Chem. Eng. J.*, 2022, **437**, 135301.
38 S. J. Zhu, W. C. Huo, X. Y. Liu and Y. X. Zhang, *Nanoscale Adv.*, 2020, **2**, 37.
39 H. Liu, W. L. Gu, B. C. Luo, P. Fan, L. B. Liao, E. K. Tian, Y. Q. Niu, J. Z. Fu, Z. Wang, Y. Y. Wu, G. C. Lv and L. F. Mei, *Electrochim. Acta*, 2018, **291**, 31.
40 H. Yi, A. M. Gao, X. K. Pang, Z. R. Ao, D. Shu, S. X. Deng, F. Y. Yi, C. He, X. P. Zhou and Z. H. Zhu, *ACS Appl. Energy Mater.*, 2020, **3**, 10192.
41 T. Xiong, M. K. Zhu, Y. X. Zhang, W. S. V. Lee, Z. G. Yu and J. M. Xue, *Batteries Supercaps*, 2020, **3**, 519.
42 G. L. Wang, Z. P. Ma, G. W. Zhang, C. Y. Li and G. J. Shao, *Electrochim. Acta*, 2015, **182**, 1070.
43 T. Q. Li, J. B. Wu, X. Xiao, B. Y. Zhang, Z. M. Hu, J. Zhou, P. H. Yang, X. Chen, B. Wang and L. Huang, *RSC Adv.*, 2016, **6**, 13914.
44 R. T. Dong, Q. L. Ye, L. L. Kuang, X. Lu, Y. Zhang, X. Zhang, G. J. Tan, Y. X. Wen and F. Wang, *ACS Appl. Mater. Interfaces*, 2013, **5**, 9508.
45 M. H. Yao, X. Ji, T. F. Chou, S. Cheng, L. F. Yang, P. Wu, H. W. Luo, Y. Y. Zhu, L. J. Tang, J. H. Wang and M. L. Liu, *ACS Appl. Energy Mater.*, 2019, **2**, 2743.
46 S. Y. Yao, R. Zhao, S. Y. Wang, Y. X. Zhou, R. C. Liu, L. Y. Hu, A. Q. Zhang, R. Yang, X. Liu, Z. N. Fu, D. W. Wang, Z. Y. Yang and Y. M. Yan, *Chem. Eng. J.*, 2022, **429**, 132521.
47 Y. Zhao, Q. Fang, X. H. Zhu, L. Xue, M. Z. Ni, C. Qiu, H. Huang, S. Sun, S. Li and H. Xia, *J. Mater. Chem. A*, 2020, **8**, 8969.
48 Y. X. Zhang, X. S. Cui, J. C. Fu, Y. P. Liu, Y. Wu, J. Y. Zhou, Z. X. Zhang and E. Q. Xie, *J. Mater. Chem. A*, 2021, **9**, 17945.
49 J. S. Lee, D. H. Shin and J. Jang, *Energy Environ. Sci.*, 2015, **8**, 3030.
50 L. J. Wu, S. J. Guo, X. J. Pu, H. W. Yue, H. Li, P. J. Li, W. Li, K. Cai, W. J. Ding, L. F. Li, Y. G. Zhang, W. J. Fa, C. C. Yang, Z. Zheng, W. W. He and Y. L. Cao, *ACS Appl. Energy Mater.*, 2022, **5**, 4505.
51 W. Qiu, Y. Li, A. You, Z. Zhang, G. Li, X. Lu and Y. Tong, *J. Mater. Chem. A*, 2017, **5**, 14838.
52 H. Yi, A. Gao, X. Pang, Z. Ao, D. Shu, S. Deng, F. Yi, C. He, X. Zhou and Z. Zhu, *ACS Appl. Energy Mater.*, 2020, **3**, 10192.
53 X. Lu, Y. Zeng, M. Yu, T. Zhai, C. Liang, S. Xie, M.-S. Balogun and Y. Tong, *Adv. Mater.*, 2014, **26**, 3148.

Published on 24 Aralk 2022. Downloaded on 9.07.2024 15:25:36.

54 J. Hou, Y. Li, L. Liu, L. Ren and X. Zhao, *J. Mater. Chem. A*, 2013, **1**, 6736.
55 Q. Wang, Y. Li, A. Serrano-Lotina, W. Han, R. Portela, R. Wang, M. A. Bañares and K. L. Yeung, *J. Am. Chem. Soc.*, 2021, **143**, 196.
56 J. Pakarinen and E. Paatero, *Miner. Eng.*, 2011, **24**, 1421.
57 B. Liu, Y. Zhang, M. Lu, Z. Su, G. Li and T. Jiang, *Miner. Eng.*, 2019, **131**, 286.
58 K. Wang, Q. Zhang, H. Hu and Y. Liu, *Hydrometallurgy*, 2019, **188**, 169.
59 X. Li, J. Ma, L. Yang, G. He, C. Zhang, R. Zhang and H. He, *Environ. Sci. Technol.*, 2018, **52**, 12685.
60 R. Cao, L. Li, P. Zhang, L. Gao and S. Rong, *Environ. Sci.: Nano*, 2021, **8**, 1628.
61 D. C. Golden, J. B. Dixon and C. C. Chen, *Clays Clay Miner.*, 1986, **34**, 511.
62 X. Li, L. Xiang, X. Xie, C. Zhang, S. Liu, Z. Li and J. Shen, *Nanotechnology*, 2020, **31**, 215406.
63 K. W. Nam, S. Kim, S. Lee, M. Salama, I. Shterenberg, Y. Gofer, J.-S. Kim, E. Yang, C. S. Park, J.-S. Kim, S.-S. Lee, W.-S. Chang, S.-G. Doo, Y. N. Jo, Y. Jung, D. Aurbach and J. W. Choi, *Nano Lett.*, 2015, **15**, 4071.
64 S. Boyd, N. R. Geise, M. F. Toney and V. Augustyn, *Front. Chem.*, 2020, **8**, 715.
65 T. Brezesinski, J. Wang, S. H. Tolbert and B. Dunn, *Nat. Mater.*, 2010, **9**, 146.
66 S. Boyd, K. Ganeshan, W.-Y. Tsai, T. Wu, S. Saeed, D.-e. Jiang, N. Balke, A. C. T. van Duin and V. Augustyn, *Nat. Mater.*, 2021, **20**, 1689.
67 K. Jayaramulu, M. Horn, A. Schneemann, H. Saini, A. Bakandritsos, V. Ranc, M. Petr, V. Stavila, C. Narayana, B. Scheibe, Š. Kment, M. Otyepka, N. Motta, D. Dubal, R. Zbořil and R. A. Fischer, *Adv. Mater.*, 2021, **33**, 2004560.
68 N. Jabeen, A. Hussain, Q. Xia, S. Sun, J. Zhu and H. Xia, *Adv. Mater.*, 2017, **29**, 1700804.
69 J. Stewart, M. D. S. Clark, J. P. Chris, J. H. Phil, I. J. P. Matt, R. Keith and M. C. Payne, *Z. Kristallogr. – Cryst. Mater.*, 2005, **220**, 567.

 This journal is © The Royal Society of Chemistry 2023